RSC Advances

PAPER

View Article Online
View Journal | View Issue

Cite this: RSC Adv., 2022, 12, 6403

Reactive synthesis and phase evolution of W_2FeB_2 alloy powders

Xin Zhou,[ab] Jun Li,[ab] Junshan Wan,[ab] Kangwei Chen,[ab] Renquan Wang[ab] and Ying Liu*[ab]

Received 17th November 2021
Accepted 8th January 2022

DOI: 10.1039/d1ra08418f

rsc.li/rsc-advances

Using industrial FeB, tungsten powder, and amorphous boron powder as raw materials, W_2FeB_2 alloy powder was successfully prepared by reaction synthesis. The reaction mechanism was analyzed by comparing the phase compositions of the alloy powder at different temperatures and holding times. The crystal structure of the W_2FeB_2 phase in the alloy powder was studied, and the content of each phase in the powder was analyzed by the density of the alloy powder. The results showed that the density of the powder obtained at 1150 °C for 3 h reached 14.32 g cm^{-3}, and the alloy powder was composed of 93.42wt% W_2FeB_2 phase with orthogonal structure and 6.58wt% W_2B phase. The reaction synthesis process involved the diffusion of B atoms and Fe atoms into the W matrix, firstly forming binary phases such as WB, W_2B, Fe_2B, W_xFe_y, and then generating ternary phases $W_xFe_yB_z$, and finally forming W_2FeB_2 phase. The powder morphology was optimized by plasma spheroidization, and the fluidity of the powders increased with the decrease of the powder feeding rate. The powder flow rate reached 19 s/50 g with a 3 g min^{-1} powder feeding rate. Metastable phases such as $(Fe_{0.6}W_{2.8})B_4$ and $W_{3.5}Fe_{2.5}B_4$ appeared after plasma spheroidization, but the phases could be eliminated with 1150 °C – 3 h annealing process.

1 Introduction

Borides, especially transition-metal borides, have high hardness and wear resistance, high melting point, excellent thermal conductivity, and chemical stabilities.[1] In the past few decades, traditional ternary transition metal borides such as Mo_2FeB_2, Mo_2NiB_2, and WCoB have been extensively studied and widely used in applications like injection molding machines parts, can molding tools, and extruding copper molds.[2–10] Ternary Fe–W–B materials also inherit the fascinating characteristics of borides[11] and show considerable application potential in these fields. However, the research on Fe–W–B system materials has been very limited so far.

Recently, FeWB alloy powders have been successfully prepared by reactive synthesis,[1] the synthesis behavior and phase evolution during the synthesis have been studied.[10,11] Amorphous Fe–W–B alloy nano-powders have been prepared by chemical reduction,[12] but Fe–W–B alloy nanopowders prepared by this method have lower crystallization temperatures, *i.e.* their thermal stability is not satisfactory. It is well known that the thermal stability of amorphous alloys affects the range of their use dramatically. W_2FeB_2, which also belongs to the Fe–W–B system, however, there is currently no report on the preparation of it. In order to conduct a systematic study of Fe–W–B system materials, it is necessary to study the W_2FeB_2 preparation method. Further, in additive manufacturing, the high fluid spherical powder is often used as raw materials to ensure the uniformity of the powder and the density of the finished parts. The preparation of spherical powders has received increasing attention due to the rapid development of additive manufacturing.[13,14] In this study, the W_2FeB_2 alloy powder was successfully prepared by reaction synthesis, the phase evolution process of the reaction was studied, and the morphology of the powders was optimized by plasma spheroidization.

2 Experimental

The commercial ferro boron (FeB) powder (20.97 wt% B, 1–3.0 μm) was obtained by mechanical crushing from ferro-boron bulk, tungsten (W) powder (99.99 wt% W, 5–15.0 μm) and amorphous boron powder (99.99 wt% B, 1–3.0 μm) were used as the raw materials. The raw materials were mixed according to the atomic ratio of Fe : W : B = 1 : 2 : 2. The ferro-boron, tungsten, and boron powders were mixed in a rotary ball-mill in ethanol together with cemented carbide balls for 24 h. The dried mixed powders were reactively synthesized in an SDZK furnace ranging from 900 °C to 1150 °C holding 0–3 h in a vacuum. And the powders were spheroidized using the Tek-15 plasma system produced by Tekna, Canada.

---

[a] College of Materials Science and Engineering, Sichuan University, Chengdu 610065, P. R. China

[b] Rare Earth and Vanadium Titanium Materials Research Center, Sichuan University, Chengdu 610065, P. R. China. E-mail: liuying5536@163.com

The phase transformation of the annealed powders was performed by X-ray diffraction (XRD) with Cu Kα irradiation ($\lambda = 0.15406$ nm) with the 2θ scan range of 20–90°. The saturation magnetization of the different alloys was tested by VSM (LakeShore 7410) to determine whether the synthesized powders contain magnetic impurity phases.

Microstructure of the powders was observed by SEM (JSM-7500F) and TEM (Talos F200S G2 S/TEM), selected area electron diffraction (SAED) measurement was used to analyze the crystal structure, and the micro-zone composition analysis was carried out using energy dispersive X-ray spectrometry (EDS) system equipped to the TEM.

The iron-containing phases in powders were analyzed by the Mössbauer spectrum. The true density of the powders was measured using a 3H-2000 TD1 true density analyzer based on Archimedes principle and gas expansion method. And the fluidity of the powders was measured by a Hall flow meter.

3 Results and discussion

3.1 Reactive synthesis of W_2FeB_2 powders

3.1.1 Synthesis temperature. Fig. 1 shows the XRD patterns of the mixed powders synthesized at various temperatures for 3 h. The phase constituents of powders synthesized at 900 °C were only FeB and W, which were consistent with the compositions of the raw material powder, the reaction synthesis process had not yet started. Since the boron powder in the raw material was amorphous, the characteristic peak of boron was not found. When the temperature increased to 950 °C, the required W_2FeB_2 phase appeared, and a small amount of WB phase also came into being, which meant the reaction synthesis process had started. But there still left a large amount of W and FeB. When the temperature further increased to 1000 °C, the W_2B phase began to form, W and WB phase disappeared in the XRD pattern, and the relative peak intensity of the W_2FeB_2 phase increased greatly. When the temperature further increased to 1050 °C, the relative peak intensity of the W_2FeB_2 diffraction peak further increased, and the relative peak intensity of the W_2B phase decreased significantly. From 1050 °C to 1150 °C, the relative peak intensity of the W_2FeB_2 phase still increased slightly, and the relative peak intensity of the W_2B phase kept falling. It suggested that the conversion of the W_2B phase to the W_2FeB_2 phase occurred with the increasing temperature from 1000 °C to 1150 °C. Combined with the appearance of the WB phase at 950 °C, it could be inferred that the WB phase firstly formed when the temperature increased, then the WB phase was transformed into W_2B, and the W_2B phase was finally transformed into the W_2FeB_2 phase.

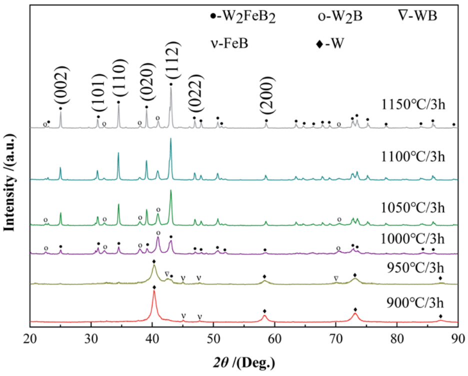

Fig. 1 XRD patterns of powders sintered at different temperatures.

The hysteresis loops of the powder were tested and the saturation magnetization was obtained by VSM. As shown in Fig. 2, the saturation magnetization of the powder was 10.43 emu g^{-1} and 10.73 emu g^{-1} at 900 °C and 950 °C, respectively, which were similar to the raw material powder. The powder was mainly composed of W and FeB phases at this temperature (Fig. 1). At 1000 °C and 1050 °C, the saturation magnetization was 4.3 emu g^{-1} and 1.27 emu g^{-1} respectively, there still was a small amount of Fe-containing magnetic phase left in the powder. It might be the Fe_2B phase that could not be detected in the XRD analysis. When the temperature increased to 1100 °C, the saturation magnetization of the powder greatly reduced to 0.19 emu g^{-1}. The powder was almost non-magnetic, indicating that the magnetic Fe-containing phase had almost reacted completely at 1100 °C, which was consistent with the reduction of the W_2B phase from 1050 °C to 1100 °C in Fig. 1. The content of the W_2B phase decreased resulting from the reaction with the magnetic FeB or Fe_2B phase. When the temperature further increased to 1150 °C, the saturation magnetization of the powder fell to 0.12 emu g^{-1}.

3.1.2 Holding time. Fig. 3 shows the XRD patterns of the powders prepared at 1150 °C with different holding time. When the holding time was 1 min, the W_2FeB_2 phase appeared. However, the diffraction peak of the WB phase was the strongest, indicating the highest content of the WB phase in the powder. In addition, Fe_2B phase was found and a little W phase remained. When the holding time increased to 1 h, the W phase disappeared, and the content of the WB phase decreased significantly, the W_2B phase began to form, and the amount of W_2FeB_2 phase increased greatly. Meanwhile, there was still a little Fe_2B left in the powder. After the holding time increased to 2 h, the characteristic peak of Fe_2B disappeared. As the holding time reached 2.5 h, the peak of the WB phase disappeared. Only W_2FeB_2 and W_2B phases existed in the powders only.

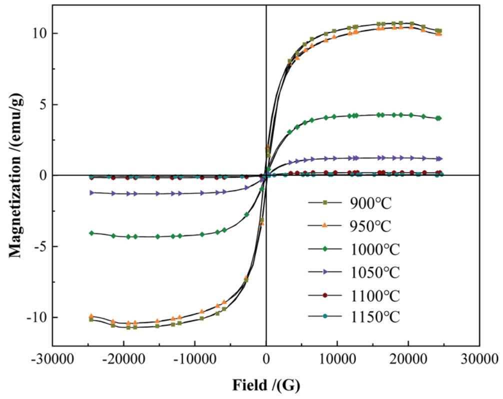

Fig. 2 The hysteresis loops of the alloy powders heat-treated at different temperatures.

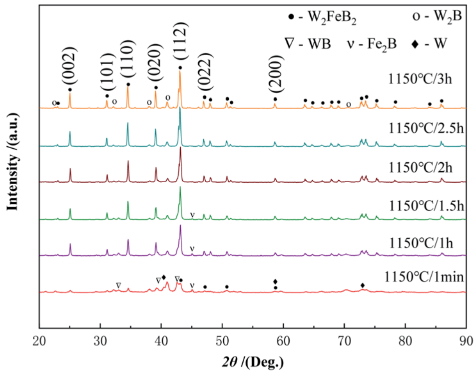

Fig. 3 XRD patterns of powders sintered with different holding time at 1150 °C.

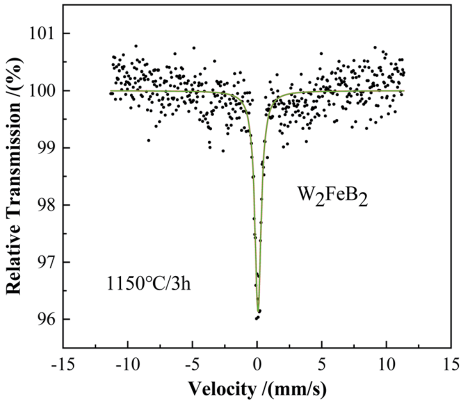

Fig. 5 Mössbauer spectra of annealed powders prepared at 1150 °C.

Table 1 Detailed Mössbauer hyperfine parameters of W_2FeB_2 powders calcined at 1150 °C

Phase	Isomer shift δ (mm s^{-1})	Quadrupole splitting Qs (mm s^{-1})	Hyperfine magnetic fields H_{hf} (KOe)	Spectrum area ratio (%)
FeW_2B_2	0	—	—	100

Fig. 4 shows the change of the saturation magnetization of the alloy powders under a different holding time. As the holding time increasing, the saturation magnetization of the alloy powders showed a significant decreasing trend. When the holding time was 1 min, the saturation magnetization was 12.04 emu g^{-1}, at this time magnetic phase Fe_2B phase existed in the powders as shown in Fig. 3. As the holding time increased to 1 h, the saturation magnetization of the powders decreased to 5.41 emu g^{-1}. Further prolonged to 1.5 h, the saturation magnetization decreased to 2.49 emu g^{-1}. When the holding time was 2 h, the saturation magnetization decreased to 0.85 emu g^{-1}, which indicated the diffraction peak of the Fe_2B phase disappeared. When the holding time continued to increase to 2.5 h, the saturation magnetization of the powder decreased to 0.19 emu g^{-1}. At this time, the diffraction peak of the WB phase disappeared according to the XRD pattern. When the holding time continues to reach 3 h, the saturation magnetization was only 0.12 emu g^{-1}.

It could be concluded that when the holding time was 1 min, WB and Fe_2B phases began to form in the powder first, and the content of W_2FeB_2 increased greatly after holding for 1 h. After holding for 2.5 h, the Fe_2B phase almost reacted completely, and the powder had scarcely any magnetism. Combined with the phase composition changes of the alloy powder at different temperatures, it could be inferred that the diffusion of B atoms occurred firstly. The B atoms in FeB diffused into the W matrix to form the WB phase and Fe_2B phase. In the subsequent reaction process, the WB phase transformed into the W_2B phase. Finally, WB and W_2B reacted with Fe_2B and transformed into the W_2FeB_2 phase. Fig. 5 and Table 1 were the Mössbauer spectra and ultra-fine parameters of the alloy powders at 1150 °C holding for 3 h. There was only one line in the spectrum, which meant that the alloy powder contained only one iron-containing phase. It was W_2FeB_2 which percentage was 100%.

Fig. 6 shows the Gibbs free energy of the raw materials and the main phases in the Fe–W–B system during the synthesis

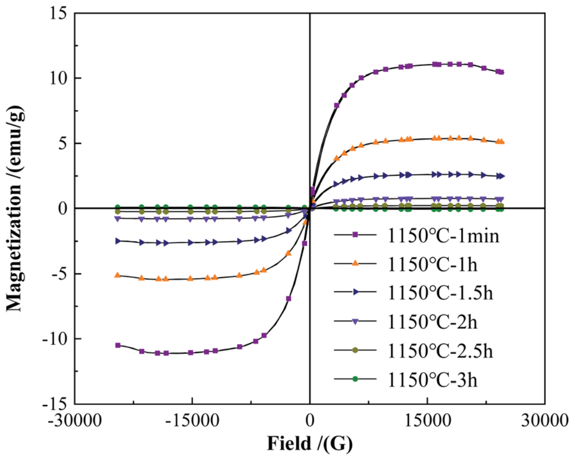

Fig. 4 The hysteresis loops of the alloy powders with different holding time.

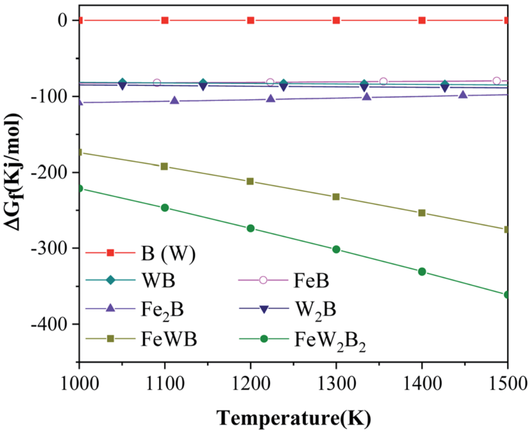

Fig. 6 Gibbs free energy of the main phases in the Fe–W–B system from 1000 K to 1500 K.

reaction at different temperatures from 1000 K to 1500 K.[15] The Gibbs free energy of W and B is 0 because they are elemental. The W_2FeB_2 phase has the lowest Gibbs free energy in the temperature range of 1000 K to 1500 K, which indicated that W_2FeB_2 is the most stable phase in this temperature range. In addition, the Gibbs free energy of W_2B and Fe_2B is lower than WB and FeB respectively, indicating that the transformation from WB and FeB to W_2B and Fe_2B meets the thermodynamic conditions.

3.2 Microstructure and true densities of alloy powder

Since the W_2FeB_2 phase might exist in forms of tetragonal or orthorhombic crystal structure,[16] so the alloy powders (1150 °C for 3 h) had been investigated by TEM in order to confirm the real crystal structure. The results in Fig. 7a and b showed the microstructure and SAED result which indicated that the alloy powder was mono-crystalline particle with size of 500 nm. Fig. 7c showed the particle consisted of Fe, W and B elements and result of the SAED pattern in Fig. 7b showed the particle was determined to be orthogonal W_2FeB_2 phase ($a = 3.146$, $b = 4.613$, $c = 7.121 < 90 \times 90 \times 90 >$, *Pmna* 62).

True densities of the alloy powders after being kept at different temperatures for 3 hours were shown in Fig. 8. The true density of the powder kept at 900 °C was 13.27 g cm^{-3}, and the counterpart at 1000 °C decreased to 13.19 g cm^{-3}. Some low-density intermediate phases formed at the beginning of the reaction. The true density rose to 14.01 g cm^{-3} at 1050 °C, combined with the XRD pattern in Fig. 1, there was a large amount of W_2FeB_2 phase in the powder at this time. At 1150 °C, the true density is further increased to 14.32 g cm^{-3}.

It could be seen from Fig. 1 and 3 that when the temperature was kept at 1150 °C for 3 hours, there were only two phases W_2FeB_2 and W_2B in the powder, and the content could be calculated by the following equation:[11]

$$x + y = 1 \tag{1}$$

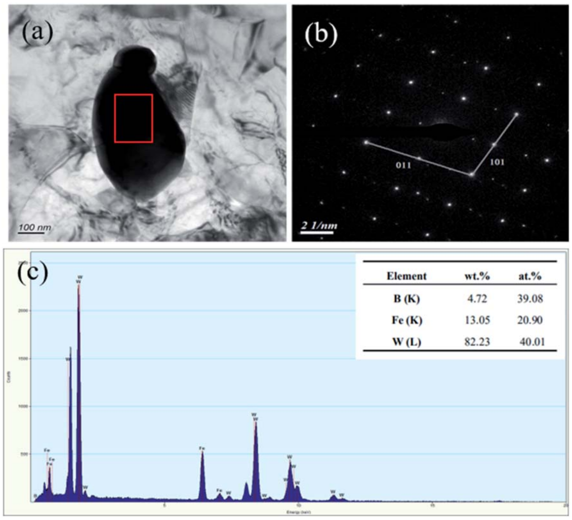

Element	wt.%	at.%
B (K)	4.72	39.08
Fe (K)	13.05	20.90
W (L)	82.23	40.01

Fig. 7 TEM results of the W_2FeB_2 particle: (a) bright-field TEM image of the particle; (b) selection electron diffraction analysis of (a); (c) EDX analysis result of the marked region.

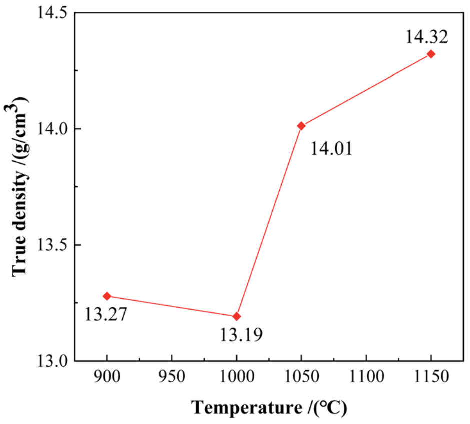

Fig. 8 Density of the powders calcined by various temperature.

$$x/\rho_x + y/\rho_y = 1/\rho_0 \tag{2}$$

x and y were the mass fractions of W_2FeB_2 and W_2B, respectively. $\rho_x = 14.16$ g cm^{-3}, $\rho_y = 17.09$ g cm^{-3}, $\rho_0 = 14.32$ g cm^{-3}. At this temperature, the content of the W_2FeB_2 phase in the powder was 93.42 wt%, and the content of the W_2B phase was 6.58 wt%.

3.3 Reactive synthesis mechanism of W_2FeB_2

To understand the intermediate phases generated in the reaction process in detail, XRD was used to analyze the powders prepared at 1000 °C with a slow scan rate (Fig. 9). It was worthy to note that the powders contained $W_{0.7}Fe_{0.3}$ ($W_{1-x}Fe_x$ type compounds, $0 \le x \le 1$) phase, $W_{1.25}Fe_{1.75}B_2$ ($W_yFe_{3\text{-}y}B_2$ type compounds, $1 \le y \le 2$), Fe_2B, and other W–B compounds. The appearance of the $W_{0.7}Fe_{0.3}$ phase was due to the diffusion of Fe atoms into the W matrix, WB and W_2B phases formed with the diffusion of B atoms into the W matrix. FeB became Fe_2B after losing the B atom. Then, the interdiffusion between these binary compounds formed some metastable ternary intermediate phases $W_yFe_{3-y}B_2$ ($1 \le y \le 2$, such as $W_{1.75}Fe_{1.25}B_2$), under this circumstance, it could be inferred that $W_{3-z}Fe_zB_2$ ($1 \le z \le 2$) type compounds were also formed during the reaction.

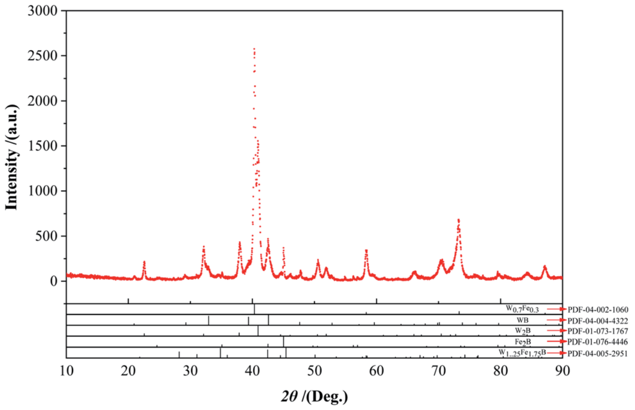

Fig. 9 XRD analyses analysis with a slow scan rate (0.02 2θ° step size) of the powders calcined at 1000 °C.

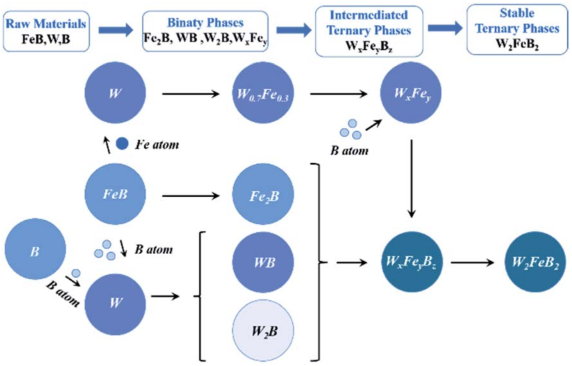

Fig. 10 Schematic diagram of the reaction synthesis.

Based on the above analysis, it was clear that W_2FeB_2 powders were transformed from binary phase (such as Fe_2B, W_2B, and $W_{0.7}Fe_{0.3}$) to metastable ternary phase ($W_xFe_yB_z$) and ultimately to the stable ternary phase (W_2FeB_2). The evolution of reactive synthesis could be briefly summarized as (Fig. 10):

$$\begin{aligned} FeB + W + B &\rightarrow WB, W_2B, Fe_2B, W_xFe_y \rightarrow W_xFe_yB_z \\ &\rightarrow W_2FeB_2 \end{aligned} \tag{3}$$

3.4 Plasma spheroidization

The morphology of the powder was observed by SEM, as shown in Fig. 11a and b. The powders were irregular. The irregular shape led to poor fluidity of the synthesized powders.

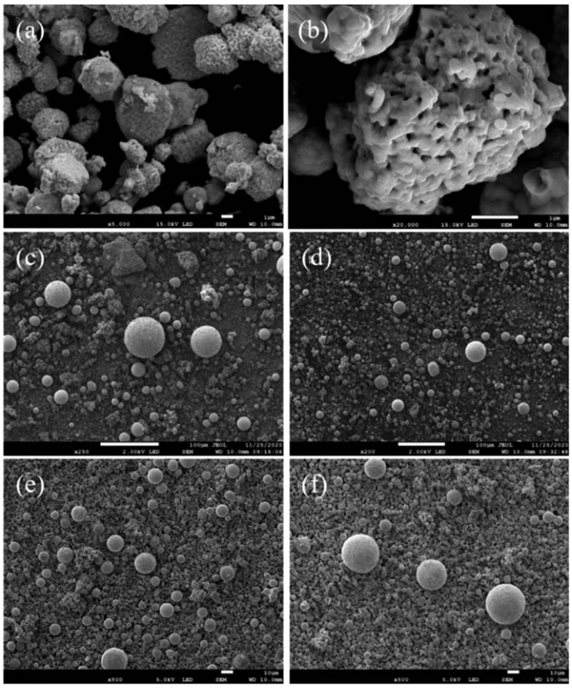

Fig. 11 SEM images the powders before and after spheroidization: (a and b) before spheroidization; (c) 33g min^{-1}; (d) 16g min^{-1}; (e) 6g min^{-1}; (f) 3g min^{-1}.

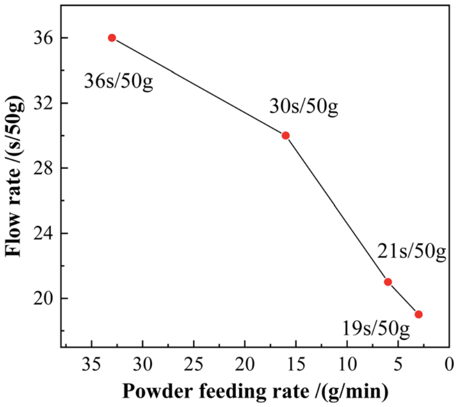

Fig. 12 Flow rates of the spheroidized powders.

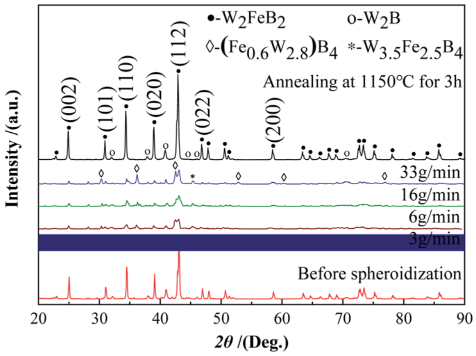

Fig. 13 XRD patterns of powders after spheroidization.

The plasma spheroidization method was used to optimize the morphology of the powders. As shown in Fig. 11c and d, when the powder feeding rate was 33 g min^{-1} and 16 g min^{-1}, the proportion of powders being spheroidized was relatively low, the particle size of the powder was uneven, and presented powder aggregation. In Fig. 11e and f, the powder feeding rate reduced to 6 g min^{-1} and 3 g min^{-1}, respectively. The proportion of the spheroidized powder increased obviously, the particle size was more uniform, and the number of agglomerates in the powders reduced. Reducing the powder feeding rate made the powders heated more uniformly in the high-temperature zone, which was beneficial to the liquefaction of the powder. Therefore, the spheroidization effect of the powder was better at a low powder feeding rate.[13,17] The fluidity of the powders after spheroidization is shown in Fig. 12. When the powder feeding rate was 3g min^{-1}, the flow rate of the powder reached 19 s/50 g.

Fig. 13 and 14 show the XRD and saturation magnetization (M_S) of the powders after spheroidization, respectively. With the powder feeding rate dropped to 3 g min^{-1}, two metastable phases appeared in the powders, which were ($Fe_{0.6}W_{2.8}$) B_4 phase and $W_{3.5}Fe_{2.5}B_4$ phase. In addition, the saturation magnetization of the powders also increased with the decrease of the powder feeding rate, indicating that the content of the magnetic phase in the powders increased. Because the powders were rapidly cooled after melting in the high-temperature zone of the plasma, the atoms in the droplets are too late to diffuse

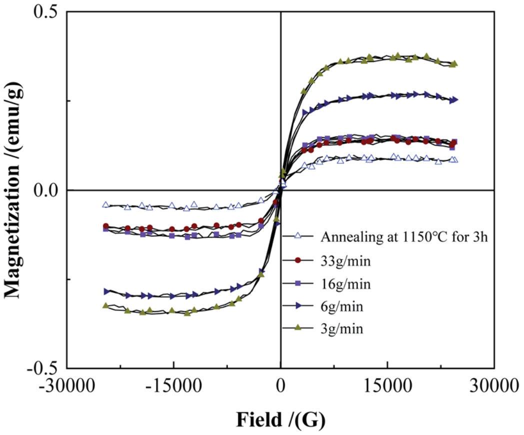

Fig. 14 Hysteresis loops of the spheroidized powders.

sufficiently, and the segregation of the metastable phases appeared consequently.

4 Conclusions

With raw materials FeB, W, and amorphous boron powder, W_2FeB_2 alloy powder could be synthesized successfully when heated at 1150 °C for 3 h. The content of the W_2FeB_2 phase and W_2B phase in the synthesized powders were 93.42 wt% and 6.58 wt% respectively. The reaction synthesis proceeded by the diffusion of B atoms and Fe atoms into the W matrix. The phase transition process of the reaction was described as follows:

$$\mathrm{Fe} + \mathrm{W} \rightarrow \mathrm{WB}, \mathrm{W_2B}, \mathrm{Fe_2B}, \mathrm{W}_x\mathrm{Fe}_y \rightarrow \mathrm{W}_x\mathrm{Fe}_y\mathrm{B}_z \rightarrow \mathrm{W_2FeB_2} \tag{4}$$

Using the plasma spheroidization method to optimize the powder morphology made the fluidity of the powder improve significantly. And the fluidity of the powder increased with the reduction of the powder feeding rate. And the segregation of components that appeared during powder spheroidization could be eliminated by annealing at 1100 °C for 3 h.

Conflicts of interest

There are no conflicts to declare.

Acknowledgements

This work is supported by the Joint Fund of the Ministry of Education [6141A020222], the Major Science and Technology Special Project of Sichuan Province [2019ZDZX001-4] and the Fundamental Research Funds for the Central Universities [YJ201910].

References

1 J. L. Li, J. Li, C. Li, *et al.* Reactive synthesis of FeWB powders and preparation of bulk materials[J], *Int. J. Refract. Met. Hard Mater.*, 2014, **46**, 80–83.

2 J. Zhang, Y. Zheng, W. Zhou, *et al.* Effects of Cr content on the microstructure and mechanical properties of Mo_2FeB_2-based cermets prepared *via* vacuum sintering[J], *Vacuum*, 2018, **155**, 509–513.

3 Y. Haizhou, L. Wenjun, F. Ping, *et al.* Synthesis and microstructure evolution during vacuum sintering of Mo_2FeB_2 based cermets[J], *Int. J. Refract. Met. Hard Mater.*, 2014, **45**, 48–52.

4 H. Yu, Y. Zheng, W. Liu, *et al.* Effect of Mn content on the microstructure and mechanical properties of Mo_2FeB_2 based cermets[J], *Int. J. Refract. Met. Hard Mater.*, 2010, **28**(2), 286–290.

5 K.-I. Takagi, W. Koike, A. Momozawa, *et al.* Effects of Cr on the properties of Mo_2NiB_2 ternary boride[J], *Solid State Sci.*, 2012, **14**(11–12), 1643–1647.

6 Y. Yamasaki, M. Nishi and K.-I. Takagi, Development of very high strength Mo_2NiB_2 complex boride base hard alloy[J], *J. Solid State Chem.*, 2004, **177**(2), 551–555.

7 J. Zhang, Y. Zheng, J. Chen, *et al.* Microstructures and mechanical properties of Mo_2FeB_2-based cermets prepared by two-step sintering technique[J], *Int. J. Refract. Met. Hard Mater.*, 2018, **72**, 56–62.

8 T. Zhang, H. Yin, C. Zhang, *et al.* First-principle calculations of mechanical properties and electronic structure of WCoB and Cr doped WCoB under high pressure[J], *Mater. Res. Express*, 2019, **6**(11), 116320.

9 T. Zhang, H. Yin, C. Zhang, *et al.* First-Principles Study on the Mechanical Properties and Electronic Structure of V Doped WCoB and W_2CoB_2 Ternary Borides[J], *Materials*, 2019, **12**(6), 967–983.

10 C. Li, J. Li, J. Li, *et al.* Study on the synthesis behavior of Fe–W–B powders and the preparation of bulk[J], *Adv. Powder Technol.*, 2015, **26**(5), 1410–1416.

11 C. Li, J. Li and Y. Liu, Phase evolution of Fe–W–B powders and stability of FeWB ternary boride prepared by reactive synthesis[J], *Mater. Res. Express*, 2018, **5**(1), 016517.

12 G. Yi, Y. Guo and B. W. Zhang, Preparation and thermal properties of amorphous Fe–W–B alloy nano-powders[J], *J. Mater. Process. Technol.*, 1998, **74**, 10–13.

13 Z. H. Hao, Z. H. Fu, J. T. Liu, *et al.* Spheroidization of a granulated molybdenum powder by radio frequency inductively coupled plasma[J], *Int. J. Refract. Met. Hard Mater.*, 2019, **82**, 15–22.

14 H. F. Gu, H. J. Gong, J. J. S. Dilip, *et al.* Effects of powder variation on the microstructure and tensile strength of ti6al4v parts fabricated by selective laser melting[J], *2014 International Solid Freeform Fabrication Symposium*, University of Texas at Austin, 2014, pp. 470-483.

15 X. Ouyang, F. Yin, J. Hu, *et al.* Experimental investigation and thermodynamic calculation of the B–Fe–W ternary system[J], *Calphad*, 2018, **63**, 212–219.

16 G. Q. Yang, H. Q. Yin, Z. F. Xu, *et al.* A first-principles-calculation exploration of ternary borides as potential alternatives to WC–Co[J], *J. Alloys Compd.*, 2019, **719**, 761–772.

17 J. He, L. Bai, H. Jin, *et al.* Optimization of tungsten particles spheroidization with different size in thermal plasma reactor based on numerical simulation[J], *Powder Technol.*, 2016, **302**, 288–297.